

# Correlations between age, kinematics, and chemistry as seen by the RAVE survey

Jennifer Wojno,<sup>1,2\*</sup> Georges Kordopatis,<sup>3</sup> Matthias Steinmetz,<sup>1</sup> Paul McMillan,<sup>4</sup> James Binney,<sup>5</sup> Benoit Famaey,<sup>6</sup> Giacomo Monari,<sup>1</sup> Ivan Minchev,<sup>1</sup> Rosemary F. G. Wyse,<sup>2</sup> Teresa Antoja,<sup>7</sup> Arnaud Siebert,<sup>6</sup> Ismael Carrillo,<sup>1</sup> Joss Bland-Hawthorn,<sup>8</sup> Eva K. Grebel,<sup>9</sup> Tomaž Zwitter,<sup>10</sup> Olivier Bienaymé,<sup>6</sup> Brad Gibson,<sup>11</sup> Andrea Kunder,<sup>12</sup> Ulisse Munari,<sup>13</sup> Julio Navarro,<sup>14</sup> Quentin Parker,<sup>15</sup> Warren Reid,<sup>16,17</sup> George Seabroke<sup>18</sup>

<sup>1</sup>Leibniz Institut für Astrophysik Potsdam, An der Sternwarte 16, 14482 Potsdam, Germany

<sup>2</sup>Department of Physics and Astronomy, Johns Hopkins University, 3400 N. Charles St, Baltimore, MD 21218, USA

<sup>3</sup>Laboratoire Lagrange, Université Côte d’Azur, Observatoire de la Côte d’Azur, Boulevard de l’Observatoire, CS 34229, 06304, Nice, France

<sup>4</sup>Lund Observatory, Lund University, Department of Astronomy and Theoretical Physics, Box 43, SE-22100 Lund, Sweden

<sup>5</sup>Rudolf Peierls Centre for Theoretical Physics, Keble Road, Oxford OX1 3NP, UK

<sup>6</sup>Observatoire astronomique de Strasbourg, Université de Strasbourg, CNRS, UMR 7550, 11 rue de l’Université, F-67000 Strasbourg, France

<sup>7</sup>Dept. FQA, Institut de Ciències del Cosmos (ICCUB), Universitat de Barcelona (IEEC-UB), Martí Franques 1, 08028 Barcelona, Spain

<sup>8</sup>Sydney Institute for Astronomy, School of Physics A28, University of Sydney, NSW 2006, Australia

<sup>9</sup>Astronomisches Rechen-Institut, Zentrum für Astronomie der Universität Heidelberg, Mönchhofstr. 12-14, D-69120 Heidelberg, Germany

<sup>10</sup>Faculty of Mathematics and Physics, University of Ljubljana, 1000 Ljubljana, Slovenia

<sup>11</sup>E.A. Milne Centre for Astrophysics, University of Hull, Hull HU6 7RX, UK

<sup>12</sup>Saint Martin’s University, 5000 Abbey Way SE, Lacey, WA 98503, USA

<sup>13</sup>INAF National Institute of Astrophysics, Astronomical Observatory of Padova, 36012 Asiago (VI), Italy

<sup>14</sup>Senior CIFAR Fellow, Department of Physics and Astronomy, University of Victoria, Victoria, BC, Canada V8P 5C2

<sup>15</sup>Department of Physics, Chong Yuet Ming Physics Building, The University of Hong Kong, Hong Kong

<sup>16</sup>Department of Physics and Astronomy, Macquarie University, Sydney, NSW 2109, Australia

<sup>17</sup>Western Sydney University, Locked Bag 1797, Penrith South, NSW 2751, Australia

<sup>18</sup>Mullard Space Science Laboratory, University College London, Holmbury St Mary, Dorking, RH5 6NT, UK

Accepted XXX. Received YYY; in original form ZZZ

## ABSTRACT

We explore the connections between stellar age, chemistry, and kinematics across a Galactocentric distance of  $7.5 < R(\text{kpc}) < 9.0$ , using a sample of  $\sim 12\,000$  intermediate-mass (FGK) turnoff stars observed with the RAdial Velocity Experiment (RAVE) survey. The kinematics of this sample are determined using radial velocity measurements from RAVE, and parallax and proper motion measurements from the Tycho-Gaia Astrometric Solution (TGAS). In addition, ages for RAVE stars are determined using a Bayesian method, taking TGAS parallaxes as a prior. We divide our sample into young ( $0 < \tau < 3$  Gyr) and old ( $8 < \tau < 13$  Gyr) populations, and then consider different metallicity bins for each of these age groups. We find significant differences in kinematic trends of young and old, metal-poor and metal-rich, stellar populations. In particular, we find a strong metallicity dependence in the mean Galactocentric radial velocity as a function of radius ( $\partial V_R / \partial R$ ) for young stars, with metal-rich stars having a much steeper gradient than metal-poor stars. For  $\partial V_\phi / \partial R$ , young, metal-rich stars significantly lag the LSR with a slightly positive gradient, while metal-poor stars show a negative gradient above the LSR. We interpret these findings as correlations between metallicity and the relative contributions of the non-axisymmetries in the Galactic gravitational potential (the spiral arms and the bar) to perturb stellar orbits.

**Key words:** Galaxy: kinematics and dynamics – Galaxy: structure – solar neighbourhood

## 1 INTRODUCTION

The field of Galactic archaeology stands poised to reveal the formation history of our Galaxy. As low- and intermediate-mass stars are long-lived, they can act as time capsules, allowing us a window to the environment in which they were born (Freeman & Bland-Hawthorn 2002). Spectroscopic surveys, such as RAVE (Steinmetz et al. 2006), SEGUE (Yanny et al. 2009), APOGEE (Majewski et al. 2017), Gaia-ESO (Gilmore et al. 2012), LAMOST (Zhao et al. 2012), and GALAH (De Silva et al. 2015), provide a number of crucial parameters necessary for disentangling the formation history of the Galactic disc, such as stellar radial velocities, effective temperatures, surface gravities, and individual chemical abundances. The precision with which we can exploit these spectra is being greatly increased by the progressive release of astrometric data from ESA’s Gaia satellite, starting with Gaia DR1 in September 2016 (Gaia Collaboration et al. 2016; Lindegren et al. 2016) and continuing with Gaia DR2 in April 2018.

It has been known for more than a century that the local velocity field is not uniform but contains moving groups (e.g. Proctor 1869; Kapteyn 1905)<sup>1</sup>: predominantly the Hyades, Pleiades, and Hercules groups. The precision of stellar velocity measurements in the solar neighbourhood has since increased dramatically, and as a result it is now possible to study this velocity space in fine detail (e.g., Dehnen 2000; Famaey et al. 2008; Williams et al. 2013; Antoja et al. 2015, 2017; Kushniruk et al. 2017; Carrillo et al. 2018). These structures are indicative of deviations of the Milky Way (MW) disc from an idealized axisymmetric model associated with our Galaxy’s bar and spiral arms. The way such structures vary in velocity space as a function Galactocentric radius has been explored in a number of simulations (e.g., Minchev et al. 2010; Quillen et al. 2011; Antoja et al. 2011; McMillan 2013; Monari et al. 2014, 2017), with a view to constraining the nature of the underlying non-axisymmetries. To understand better the dynamical processes that shape the kinematic trends we see in stellar populations today, we turn to measurements of the local mean stellar velocity field  $\mathbf{V}$ , which we analyse in Galactocentric cylindrical polar coordinates  $(R, \phi, z)$ .

Siebert et al. (2011) first detected a gradient in  $V_R$ , namely  $\partial V_R / \partial R \lesssim -3 \text{ km s}^{-1} \text{ kpc}^{-1}$ , using the line-of-sight velocities of RAVE stars. Siebert et al. (2012) fitted this shallow gradient to a model on the assumption that it is solely due to long-lived spiral arms. They found that they were able to reproduce the observational results with a two-armed model in the solar neighbourhood ( $d < 1 \text{ kpc}$ ), although they acknowledged that the bar could contribute. Monari et al. (2014) developed a model of the bar’s contribution to the velocity field near the Sun. They showed that if the Sun is located close to the bar’s outer Lindblad resonance (OLR), from our position we would measure a trend similar to that found in Williams et al. (2013), which measured a slightly steeper gradient,  $\partial V_R / \partial R = -8 \text{ km s}^{-1} \text{ kpc}^{-1}$ . Grand et al. (2012) analysing N-body simulations and Monari et al. (2016), modelling spiral arms with linear perturbation theory, showed that stars located in arms move in toward the

Galactic centre, while stars in interarm regions move outwards. Monari et al. (2016) estimated the gradient in the data to be  $\partial V_R / \partial R \simeq -8 \text{ km s}^{-1} \text{ kpc}^{-1}$ .

The study by Faure et al. (2014) of the combined effect of the bar and spiral arms noted that the pattern just described in which stars in arms move inwards reverses outside the corotation resonance, so there stars in arms move outwards while stars between arms move inwards. This finding is consistent with the perturbative model of Monari et al. (2016).

Soon after the gradient in  $V_R$  was found in RAVE stars, Widrow et al. (2012) discovered significant deviations in  $V_z$  with height  $z$  above the plane using the Sloan Digital Sky Survey (SDSS). Using the high-resolution simulation of Purcell et al. (2011) to study of the effect of the Sagittarius dwarf spheroidal galaxy (dSph) on the MW disc, Gómez et al. (2013) concluded that by plunging through the disc  $\sim 2 \text{ Gyr}$  ago, the Sagittarius dSph could have generated the pattern in  $V_z$  detected by Widrow et al. (2012). Carlin et al. (2013) found a similar signature in LAMOST stars that are distributed through a larger volume. Williams et al. (2013) analysed the  $V_z$  field defined by RAVE stars, and detected wave-like motions perpendicular to the plane that could either be associated with spiral arms or with a recent accretion event. However, Carrillo et al. (2018), reanalysing the RAVE data, laid bare the extent to which the small measured values of  $V_z$  are vulnerable to systematic errors in both proper motions and distances. Using TGAS proper motions and improved distances, they concluded that vertical motions inside the solar radius could be induced by the Galactic bar or spiral arms, while outside they are likely generated by a recent satellite/merging event.

Recently, Antoja et al. (2017) investigated the dependence of the velocity field on metallicity. In a novel analysis applied to data from RAVE and the Geneva-Copenhagen Survey (GCS, Holmberg et al. 2007) they compared the metallicity distribution at  $(V_R, V_\phi)$  with that at  $(-V_R, V_\phi)$ , which would be identical in a well-mixed axisymmetric model. The fact that the observed metallicity distributions differed is consistent with previous studies (e.g., Famaey et al. 2007) that have shown that the chemical abundances of moving groups differs from that of the local interstellar medium (ISM). In particular, moving groups are not chemically homogeneous, so they cannot be dissolved open clusters.

A significant barrier to uncovering the chemodynamical history of the solar neighbourhood is the difficulty of determining the ages of individual field stars. The classical approach to age determination involves measuring the luminosity of turnoff stars of known colour and metallicity. This method requires an accurate distance. We now have trigonometric parallaxes from the Tycho-Gaia Astrometric Solution (TGAS) (Gaia Collaboration et al. 2016; Lindegren et al. 2016) for two million stars, so we can determine credible ages for large samples of stars. Here we combine TGAS parallaxes and proper motions with RAVE spectroscopy of turnoff stars to discover how the velocity field depends on age and metallicity.

In Section 2 we review the RAVE survey and its updated distance pipeline from which our distances and ages are derived (Section 2.2). In Section 2.3 we record the criteria used to select our samples and the steps taken to val-

<sup>1</sup> For a history of the discovery of moving groups see Antoja et al. (2010).

idate our ages. With our sample of stars in hand, we then explore kinematic trends, in particular  $\partial V_{R,\phi}/\partial R$  for two selected age bins (young and old) in Section 3, as a function of Galactocentric radius. Section 4 presents the distributions of orbital parameters for our age-metallicity bins. In Section 5 we present a discussion and interpretation of our results, and draw our conclusions from this analysis.

## 2 THE DATA

### 2.1 The RAVE survey

The RAVE survey collected over half a million medium-resolution ( $R \approx 7500$ ) spectra of stars in the Southern hemisphere from 2003 until 2013, using the 6dF multi-object spectrograph on the 1.2-m UK Schmidt Telescope at the Siding Spring Observatory in Australia. Throughout the course of the survey, parameters derived from the spectra were made publicly available via a number of data releases, with the fifth data release (DR5) being the latest (Kunder et al. 2017), providing 520 781 measurements for 457 588 individual stars. Centred on the Ca II-triplet region (8410 – 8795 Å) region, this spectral range was chosen specifically to coincide with the spectral range of Gaia’s Radial Velocity Spectrometer (RVS) (Prusti 2012; Bailer-Jones et al. 2013; Recio-Blanco et al. 2016).

In addition to radial velocities (typical uncertainties  $\sim 2 \text{ km s}^{-1}$ , Kunder et al. 2017; Kordopatis et al. 2013a), RAVE DR5 contains a number of other stellar parameters derived from spectra including effective temperature, surface gravity, metallicity ( $[M/H]$ ), as well as individual abundances for six elements (Mg, Al, Si, Ti, Fe, Ni) (Boeche et al. 2011). To provide additional parameters such as apparent magnitudes and proper motions, RAVE DR5 was cross-matched with a number of other astrometric and photometric catalogues. In particular, RAVE has a significant overlap with stars available in TGAS (Lindgren et al. 2016), with RAVE DR5 containing 215 590 unique TGAS stars. Currently, the RAVE survey offers one of the largest samples of stars with accurate 6D phase-space information in addition to stellar parameters derived from spectra.

### 2.2 Distances and ages

We use distances and ages returned by an updated version of the pipeline described in Binney et al. (2014), details of which are given in McMillan et al. (2017). The updated pipeline allows for TGAS parallaxes to be included as priors, alongside stellar parameters such as temperature, surface gravity, and metallicity from RAVE, apparent magnitudes from 2MASS (Skrutskie et al. 2006) and AllWISE (Cutri et al. 2013), and an underlying Galactic model. The default Galactic model (prior) used is the same as that used for the distance determinations available in DR4 and DR5 and includes priors on stellar metallicities and ages for a given disc component (McMillan et al. 2017, Section 2.1). Details of the other available priors can be found in Section 5 of McMillan et al. (2017). From both internal tests and comparisons with external catalogues, McMillan et al. (2017) report that the combined spectrophotometric distance es-

timates perform better than purely spectroscopic or astrometric estimates.

In addition to distance estimates, the updated pipeline produces estimates of stellar mass, metallicity, line of sight extinction, and age as byproducts. For this work, we want to avoid a prior where a relationship between age and metallicity is imposed. Therefore, we use age estimates derived utilizing a Galactic model with a flat prior on both age and metallicity (‘Density’ in McMillan et al. 2017). The ages derived using this prior are roughly consistent with those derived using an age prior where the star formation rate declines over time (McMillan et al. 2017, Equation 20), and a flat prior in metallicity. Derived distances are not significantly affected by the choice of prior.

### 2.3 Age validation

To validate the pipeline’s age estimates, we generate a mock catalogue of RAVE-like stars using the population synthesis code GALAXIA (Sharma et al. 2011). As GALAXIA uses PARSEC (Bressan et al. 2012) isochrones to produce stars with perfectly-known ages and atmospheric parameters ( $T_{\text{eff}}$ ,  $\log g$ ,  $[M/H]$ ), 2MASS photometry, and distances, it offers a suitable test sample for assessing internal uncertainties on the output of the distance pipeline.

#### 2.3.1 Mock catalogue generation

We generated stars with I-magnitude range  $7 < I_{\text{DENIS}} < 13$ , to cover the whole magnitude range of RAVE, and removed all stars with Galactic latitudes  $|b| < 5^\circ$ . We then resampled the age distribution of our mock catalogue (primarily by reducing the number of young stars) to ensure we had enough stars for robust statistics across the entire range of stellar ages, and as a side-effect, roughly reproduce the age distribution of the extended solar neighbourhood.

#### 2.3.2 Applying uncertainties to our mock catalogue

We then scattered the mock data for  $T_{\text{eff}}$ ,  $\log g$ , and  $[M/H]$  by RAVE-like uncertainties. The standard deviations used in this process were the quadrature sums of RAVE’s internal and external uncertainties for a star with the given true data (for more detail see Figure 5 of Wojno et al. 2017).

The true apparent magnitudes  $J$ ,  $H$  and  $K_s$  in the mock data were then scattered by a Gaussian error distribution with dispersion 0.025 mag, which is a typical 2MASS uncertainty. Finally, the true parallaxes were scattered by a Gaussian error distribution with a dispersion of 0.3 mas, which is a typical TGAS uncertainty (Gaia Collaboration et al. 2016; Lindgren et al. 2016).

#### 2.3.3 Input versus output age comparison

The mock data were then fed into the updated RAVE distance pipeline and the resulting ages compared with the ‘true’ ages given by GALAXIA. As a preliminary sanity check the values of  $T_{\text{eff}}$ ,  $\log g$ ,  $[M/H]$  and distance from the pipeline were compared with the original values from GALAXIA and found to agree within the errors. Figure 1 shows the input and output ages subdivided by regions within the  $T_{\text{eff}} - \log g$

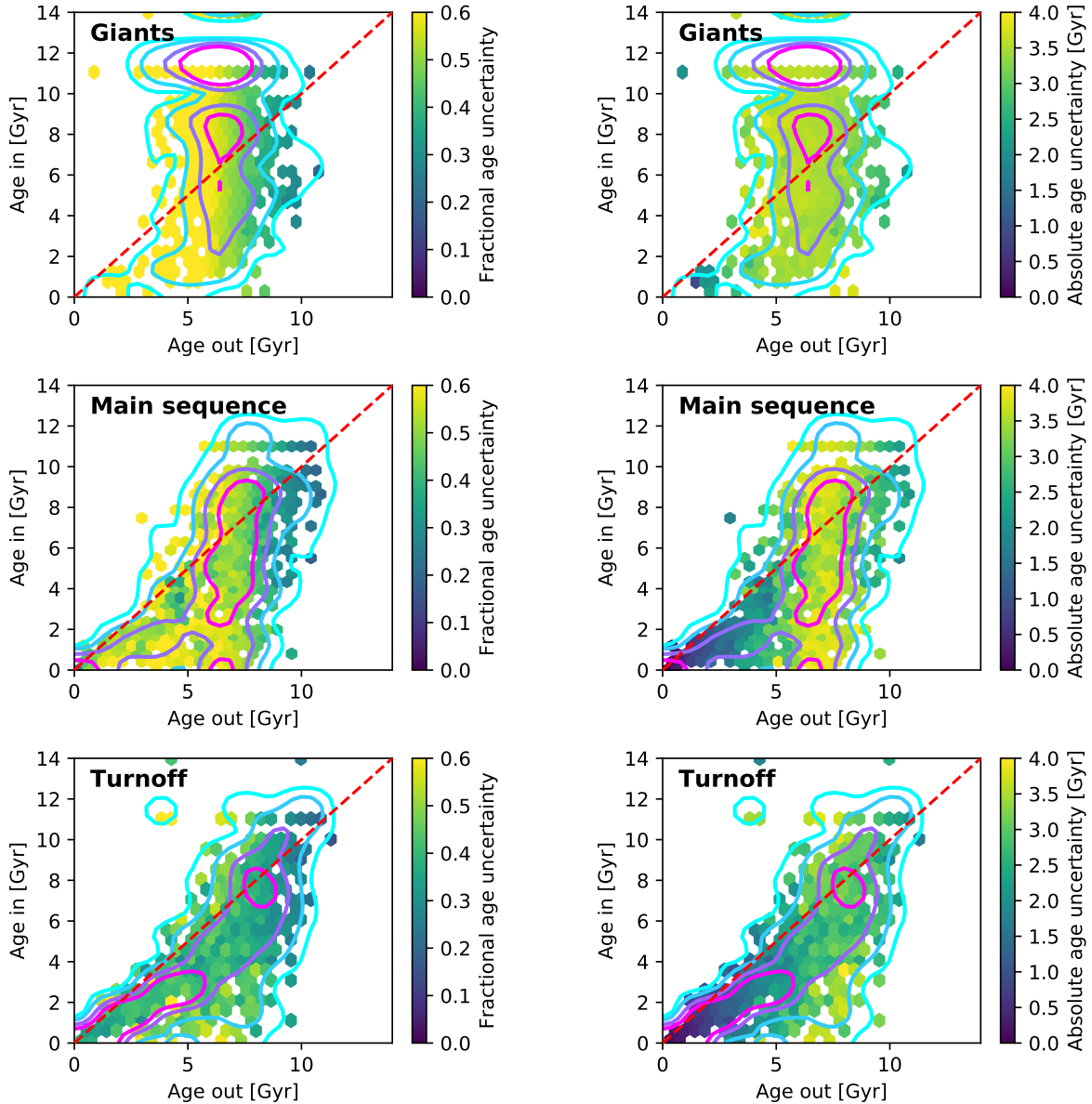


**Figure 1.** Input age vs. output age, with bins coloured by fractional age uncertainty in the left column, and by absolute age uncertainty in the right column. Giants ( $T_{\text{eff}} < 5500$  K,  $\log g < 3.5$ ), main sequence stars ( $\log g > 4.25$ ), and turn off stars ( $T_{\text{eff}} > 5500$  K,  $3.5 < \log g < 4.25$ ) are shown as the top, middle, and bottom rows, respectively. Contours indicate 33, 67, 90, and 99 per cent of the sample.

plane. The top row shows the data for giant stars ( $T_{\text{eff}} < 5500$  K,  $\log g < 3.5$ ), the middle row shows the data for main-sequence stars ( $\log g > 4.25$ ), and the bottom row shows the data for turnoff stars ( $5500 \text{ K} < T_{\text{eff}} < 7100 \text{ K}$ ,  $3.5 < \log g < 4.25$ ). Panels in the left column are colour-coded by fractional age uncertainty, while panels on the right are colour-coded by absolute age uncertainty. The contours enclose 33, 67, 90, and 99 per cent of the sample. Unsurprisingly, the giant and main-sequence samples have much higher uncertainties than the turnoff sample, with almost all stars being assigned an intermediate age regardless of its true age. Consequently, we exclude all but turnoff stars from further consideration. For turnoff stars, the isochrones are much better separated than for the giant and lower main-

sequence stars, and therefore yield smaller age uncertainties (see Figure 3).

In order to obtain a balanced sample with the most precise age estimates possible, we restrict further analysis to turnoff stars in two age bins: young ( $0 < \tau < 3$  Gyr) and old ( $8 < \tau < 13$  Gyr) stars. We do not use stars of intermediate-age ( $3 < \tau < 8$  Gyr) because this age group manifests a significant systematic offset. While this offset disappears if we only consider stars with age uncertainties less than 20%, we find that this prunes the sample in a biased way. Intermediate-age stars are more likely to have large age uncertainties because their errors are unrestricted: a young star cannot have an age smaller than zero, and an old star cannot have an age that exceeds 13.8 Gyr.



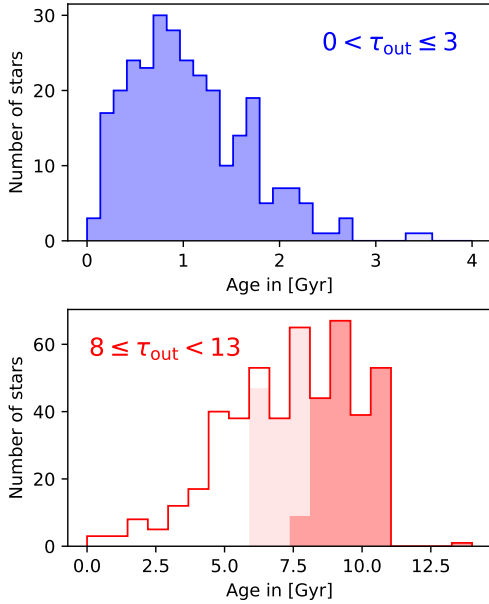


**Figure 2.** Distribution of input ages for the stars with output ages given by the range indicated in the plot. The top panel shows the distribution for our ‘young’ sample, while the bottom panel shows the distribution for our ‘old’ sample. The darker shaded regions indicate stars with input ages that fall within the given bin, while the lighter shaded regions indicate stars with input ages that fall slightly outside of the given bin. A lack of shading indicates stars which are considered contaminants of that bin.

#### 2.3.4 Contamination

We now estimate the number of stars that wrongly appear in the ‘young’ and ‘old’ bins as a consequence of observational and theoretical uncertainties. In Figure 2, we show the distributions of input ages of stars that end up in the young ( $0 < \tau < 3$  Gyr) and old ( $8 < \tau < 13$  Gyr) bins. The dark-shaded areas are regions within which the star has been correctly classified as young or old. The lighter-shaded areas indicate regions in which the star is not as young or old as its bin membership implies, but is nonetheless pretty young ( $\tau \leq 4$  Gyr) if it is in the young bin, or pretty old ( $\tau \geq 6$  Gyr) if it is in the old bin. From this analysis we conclude that our ‘young’ sample has a success rate of  $\sim 98$  per cent in the sense that less than  $\sim 2$  per cent of its stars are older than 4 Gyr, and our ‘old’ sample has a success rate of  $\sim 73$  per cent in the sense that less than  $\sim 27$  per cent of its stars are younger than 6 Gyr.

### 2.4 Selection of our RAVE-TGAS sample

In light of the work presented in the last section, henceforth we confine our analysis to the 37765 RAVE turnoff stars ( $5500 < T_{\text{eff}} < 7100$  K,  $3.5 < \log g < 4.25$ ). This selection in  $T_{\text{eff}} - \log g$  space is shown in Figure 3 by the dashed red lines. Pixels in Figure 3 are colour-coded by fractional age uncertainty, with solar-metallicity isochrones overplotted in black, spanning a range in age from 1 to 13 Gyr in steps of 1 Gyr.

A histogram of the age uncertainties for this sample is shown in Figure 4. The majority of our sample ( $\sim 60$  per

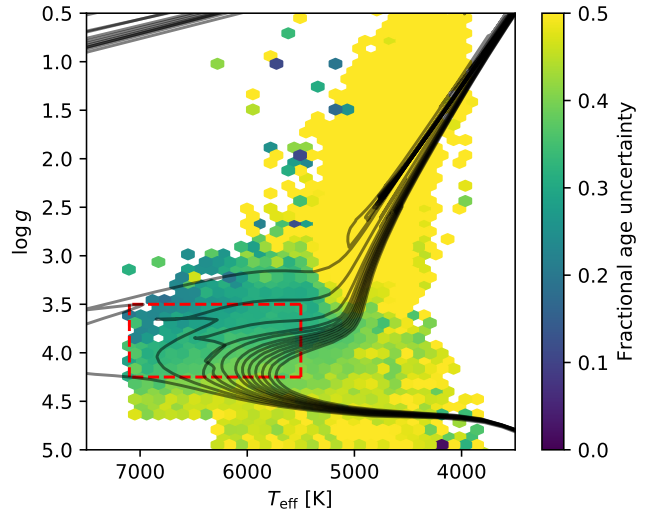


**Figure 3.** Spectroscopic  $T_{\text{eff}} - \log g$  diagram of RAVE DR5 stars which satisfy the quality criteria listed in Sec. 2.4.1. The dashed red lines indicate the cuts made in the parameter space to select for only turnoff stars. The bins are colour-coded by the fractional age uncertainty. Solar-metallicity isochrones are overplotted in black, and span a range in age from 1 to 13 Gyr, with a step size of  $\sim 1$  Gyr.

cent) has age uncertainties less than 2 Gyr, with a sizable fraction ( $\sim 25$  per cent) having age uncertainties less than 1 Gyr.

#### 2.4.1 RAVE quality criteria

We further restrict analysis to stars that have: a high signal-to-noise ratio (SNR\_K); a reasonable estimate for their line-of-sight velocity (eHRV); reliable atmospheric parameters because (i) the stellar-parameter pipeline converged (Algo\_Conv\_K, Kordopatis et al. 2013a), and (ii) the fit between the best-fitting model and the observed spectrum from the chemical pipeline (CHISQ\_c, Boeche et al. 2011) was reasonable. In addition, we remove peculiar stars flagged by the classification pipeline as having anomalous spectra (Matijević et al. 2012). Quantitatively, we require:

- $\text{SNR\_K} > 40$
- $\text{eHRV} < 8 \text{ km s}^{-1}$
- $\text{Algo\_Conv\_K} \neq 1$
- $\text{CHISQ\_c} < 2000$
- $\text{c1} = \text{d, g, h, n, or o}$
- $\text{c2} = \text{d, g, h, n, o, or e}$
- $\text{c3} = \text{d, g, h, n, o, or e}$

We then apply the age bins described in Sec. 2.3.3: young ( $0 < \tau < 3$  Gyr) and old ( $8 < \tau < 13$  Gyr), to this sample of turnoff stars. After applying these criteria, we are left with 6630 ‘young’ stars and 5072 ‘old’ stars. The spatial distributions of our selected young and old populations are shown in Figure 5, with blue and red contours, respectively.

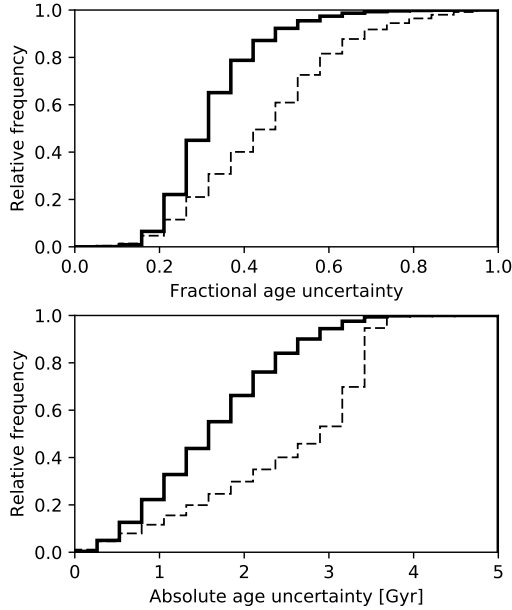


**Figure 4.** Cumulative histogram of the fractional (top) and absolute (bottom) age uncertainties of our final selected sample of turnoff stars (solid line), and for the whole RAVE-TGAS sample (dashed line).

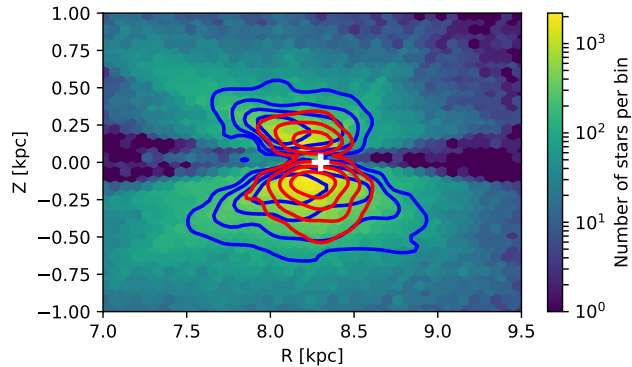


**Figure 5.** Spatial extent of the selected young (blue contours) and old (red contours) turnoff stars. Contours indicate 33, 67, 90, and 99 per cent of each sample. The spatial extent and density of the entire RAVE-TGAS sample (i.e., all spectral types) is shown by the 2D histogram beneath. The white plus indicates the position of the Sun.

#### 2.4.2 Metallicity bins

We divide each age group into the four metallicity bins illustrated in Figure 6. The bins are:

- Bins 1 and 5:  $0.15 \leq [\text{Fe}/\text{H}] < 0.45$
- Bins 2 and 6:  $-0.15 \leq [\text{Fe}/\text{H}] < 0.15$
- Bins 3 and 7:  $-0.45 \leq [\text{Fe}/\text{H}] < -0.15$
- Bins 4 and 8:  $-0.75 \leq [\text{Fe}/\text{H}] < -0.45$

Throughout the rest of the text, we will refer to these bins by the numbers listed above and shown in Figure 6. We note that the radial distribution of stars does not vary significantly between these metallicity bins, for both the young

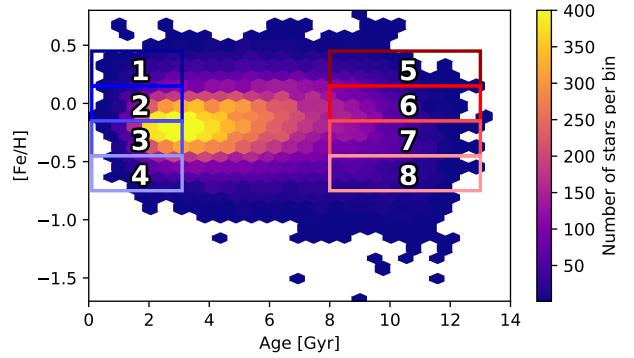


**Figure 6.** Age vs.  $[\text{Fe}/\text{H}]$  2D histogram for our sample of turnoff stars defined by the red dashed lines in Figure 3, colour-coded by density. We consider four metallicity bins for each age group, described in Section 2.4.2.

(Bins 1-4) and old (Bins 5-8) samples. Our young sample has a Galactocentric radial distribution that peaks at  $R \sim 8.2$  kpc, with  $\sigma_R \sim 0.25$  kpc, and for old stars,  $R \sim 8.25$  kpc and  $\sigma_R \sim 0.12$  kpc (see Figure 5).

### 3 VELOCITY DISTRIBUTIONS

We now examine for each of the eight age–metallicity bins marked in Fig. 6 the distributions of  $V_R$ ,  $V_\phi$  and  $V_z$ . We determine Galactocentric velocities in cylindrical coordinates following Appendix A of Williams et al. (2013) with the location of the Sun taken to be  $(R_0, z_0) = (8.3, 0)$  kpc, and the local circular speed to be  $V_{\text{LSR}} = 240 \text{ km s}^{-1}$  (Schönrich 2012), and the solar peculiar velocity to be  $(U, V, W)_\odot = (11.10, 12.24, 7.25) \text{ km s}^{-1}$  (Schönrich et al. 2010).  $V_R$  is positive for motion away from the Galactic centre,  $V_\phi$  is positive in the direction of Galactic rotation, and  $V_z$  is positive towards the north Galactic pole. Line-of-sight velocities are provided by RAVE DR5 (Kunder et al. 2017), and proper motions are taken from the TGAS catalogue (Lindgren et al. 2016).

#### 3.1 Correcting by the selection function of RAVE

As RAVE is not a volume-complete survey, when computing kinematic trends we need to correct for the selection function. Wojno et al. (2017) and references therein show that the selection function of RAVE is relatively simple and well-behaved in the sense that RAVE is not kinematically or chemically biased wherever its stellar parameter pipeline gives reliable results. However, our sample comprises exclusively stars contained in both RAVE and TGAS, which had vastly different observing strategies and sky completeness, and therefore we had to reevaluate the selection function  $S_{\text{select}}$ . We computed  $S_{\text{select}}$  as a function of position on the sky in HEALPIX (Górski et al. 2005) pixels,  $I_{2\text{MASS}}$  magnitude, and  $(J - K_s)$  colour from the definition

$$S_{\text{select}}(\text{pixel}_{\alpha,\delta}) = \frac{\sum \sum N_{\text{RAVE}}(\text{pixel}_{\alpha,\delta}, I, J - K_s)}{\sum \sum N_{2\text{MASS}}(\text{pixel}_{\alpha,\delta}, I, J - K_s)}. \quad (1)$$

Each star contributes to the statistical analysis with a weight  $w_i = 1/S_{\text{select}}$  in the sense that the weighted mean  $\bar{x}$  and

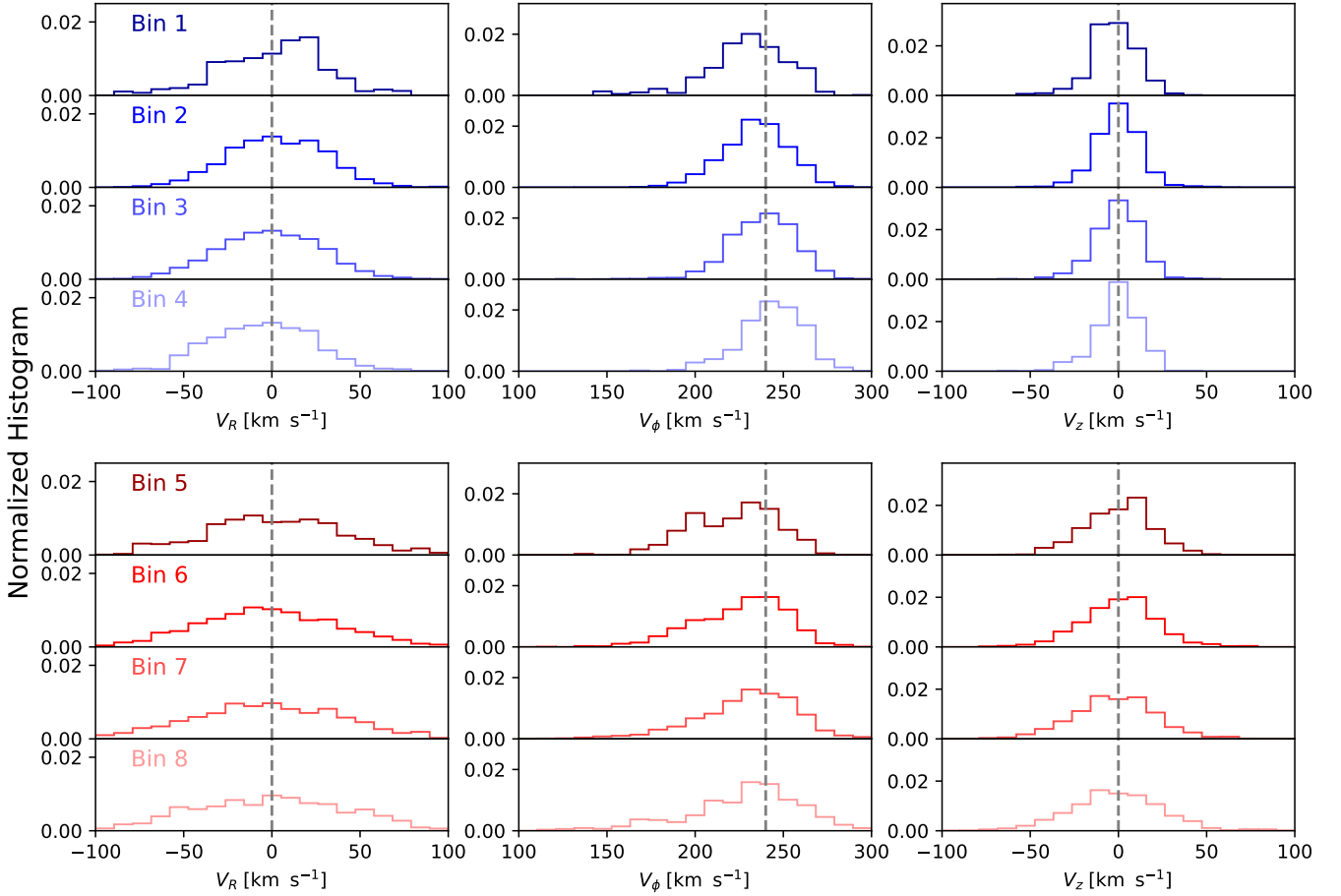


**Figure 7.** Cylindrical velocity distributions (left to right:  $V_R$ ,  $V_\phi$ ,  $V_z$ ), weighted by the selection function, for our two age bins. Young stars are plotted in blue, old stars are plotted in red. More metal-rich bins are plotted with darker colours, with more metal-poor bins in lighter colours (metallicity Bins 1, 2, 3, and 4 for young stars, and Bins 5, 6, 7, and 8 for old stars). Grey dashed lines indicate  $0 \text{ km s}^{-1}$  for the  $V_R$  and  $V_z$  components, and  $240 \text{ km s}^{-1}$  for the  $V_\phi$  component.

**Table 1.** Mean and dispersion for each component of the Galactocentric cylindrical velocity, weighted by the selection function, for both age groups and each metallicity bin within the age groups.

Bin number	Metallicity range	N	$\overline{V_R}$	$\sigma_R$	$\overline{V_\phi}$	$\sigma_\phi$	$\overline{V_z}$	$\sigma_z$
Young								
1	$0.15 \leq [\text{Fe}/\text{H}] < 0.45$	386	$0.5 \pm 1.3$	$30.3 \pm 1.1$	$229.3 \pm 1.0$	$23.6 \pm 0.8$	$-2.4 \pm 0.5$	$12.8 \pm 0.5$
2	$-0.15 \leq [\text{Fe}/\text{H}] < 0.15$	2534	$2.1 \pm 0.4$	$27.2 \pm 0.4$	$234.0 \pm 0.3$	$18.4 \pm 0.3$	$-0.2 \pm 0.2$	$12.9 \pm 0.2$
3	$-0.45 \leq [\text{Fe}/\text{H}] < -0.15$	3141	$-1.8 \pm 0.4$	$30.1 \pm 0.4$	$237.7 \pm 0.3$	$18.6 \pm 0.2$	$-0.3 \pm 0.2$	$13.2 \pm 0.2$
4	$-0.75 \leq [\text{Fe}/\text{H}] < -0.45$	542	$-5.6 \pm 1.0$	$29.2 \pm 0.9$	$243.2 \pm 0.6$	$18.0 \pm 0.5$	$0.1 \pm 0.5$	$12.6 \pm 0.4$
Old								
5	$0.15 \leq [\text{Fe}/\text{H}] < 0.45$	531	$0.4 \pm 1.4$	$39.3 \pm 0.6$	$222.1 \pm 0.9$	$24.4 \pm 0.9$	$0.1 \pm 0.7$	$19.0 \pm 1.2$
6	$-0.15 \leq [\text{Fe}/\text{H}] < 0.15$	1757	$-2.2 \pm 0.8$	$40.5 \pm 1.0$	$225.6 \pm 0.5$	$25.8 \pm 1.6$	$0.5 \pm 0.4$	$21.2 \pm 2.0$
7	$-0.45 \leq [\text{Fe}/\text{H}] < -0.15$	1740	$-2.6 \pm 0.8$	$43.2 \pm 1.0$	$228.7 \pm 0.6$	$28.9 \pm 1.4$	$-2.2 \pm 0.5$	$24.3 \pm 1.7$
8	$-0.75 \leq [\text{Fe}/\text{H}] < -0.45$	838	$-2.5 \pm 1.3$	$47.2 \pm 0.6$	$227.5 \pm 0.9$	$32.9 \pm 0.9$	$-1.6 \pm 0.8$	$27.3 \pm 1.0$

weighted dispersion  $\sigma_x$  of an observable  $x$  are

$$\bar{x} = \frac{\sum_{i=1}^n (x_i \times w_i)}{\sum_{i=1}^n w_i} \quad (2)$$

$$\sigma_x^2 = \frac{\sum_{i=1}^n w_i (x_i - \bar{x})^2}{k \sum_{i=1}^n w_i}, \quad (3)$$

where  $k = (N' - 1)/N'$ , and  $N'$  is the number of non-zero weights.

### 3.2 Velocity trends with age and $[\text{Fe}/\text{H}]$

Figure 7 shows (left to right) the weighted distributions of  $V_R$ ,  $V_\phi$  and  $V_z$  for stars in the young bin (blue, top row), and

the old bin (red, bottom row), with each age bin divided into the four metallicity bins defined in Fig. 6. Statistics for each histogram, computed according to equations (2) and (3), are given in Table 1. We note that the values of  $\sigma_{R,\phi,z}$  given in Table 1 have been corrected for the contribution of observational uncertainties:

$$\sigma_{R,\phi,z} = \sqrt{\sigma_{R,\phi,z}^2 - e_{V_{R,\phi,z}}^2} \quad (4)$$

where  $e_{V_{R,\phi,z}}$  is the reported uncertainty for each component of the velocity, weighted by the selection function.

The values in Table 1 for young stars (upper block) show that  $V_R$  and  $V_z$  do not vary significantly with metallicity. By contrast  $V_\phi$  increases as  $[\text{Fe}/\text{H}]$  decreases. An inverse correlation of  $V_\phi$  with  $[\text{Fe}/\text{H}]$  within the thin disc is well known (e.g. Lee et al. 2011; Adibekyan et al. 2013; Recio-Blanco et al. 2014; Wojno et al. 2016; Kordopatis et al. 2017), and recognised to be a signature of the metallicity gradient within the thin disc (e.g. Schönrich et al. 2010): metal-poor stars tend to have large guiding-centre radii and to visit us near pericentre, whereas metal-rich stars tend to have small guiding-centre radii and visit us near apocentre. Quantitatively, we find

$$\frac{\partial V_\phi}{\partial [\text{Fe}/\text{H}]} \approx -15 \text{ km s}^{-1} \text{ dex}^{-1} \quad (\text{young stars}). \quad (5)$$

We estimate this value by a simple linear fit to the values of  $\overline{V_\phi}$  for the four metallicity bins, taking the center of the metallicity bin for the value on the x-axis. Previous estimates of  $\partial V_\phi / \partial [\text{Fe}/\text{H}]$  have ranged from  $-23 \text{ km s}^{-1} \text{ dex}^{-1}$  to  $-11 \text{ km s}^{-1} \text{ dex}^{-1}$ . While our estimate is comparable, literature values usually indicate a steeper gradient than we find.

Table 1 indicates that  $\sigma_\phi$  decreases as metallicity decreases, with Bin 1 having a dispersion  $\sigma_\phi = 23.6 \pm 0.8 \text{ km s}^{-1}$  and Bin 4 having  $\sigma_\phi = 18.0 \pm 0.5 \text{ km s}^{-1}$ . This trend is a natural corollary of an increase in mean Galactocentric radius with decreasing metallicity and the stellar disc becoming cooler as one moves outward. The data for  $\sigma_R$  suggest, however, that we treat the trend in  $\sigma_\phi$  with caution because they do not show a corresponding decrease while dynamical theory requires  $\sigma_R$  and  $\sigma_\phi$  to vary together.

In line with much previous work (e.g., Nordström et al. 2004; Guiglion et al. 2015) the histograms for old stars are broader than those for young stars. All three velocity dispersions increase with decreasing  $[\text{Fe}/\text{H}]$ , so amongst old stars the metal-poor component is the hottest – this is the reverse of the trend in  $\sigma_\phi$  that we just saw in the young stars. Gratifyingly, the data for  $V_\phi$  for old stars show it to decrease as  $[\text{Fe}/\text{H}]$  increases, just as dynamical theory requires given the increase in  $\sigma_\phi$ . Many previous studies (e.g. Spagna et al. 2010; Kordopatis et al. 2011; Adibekyan et al. 2013; Kordopatis et al. 2013b; Wojno et al. 2016; Kordopatis et al. 2017) have found the same trend of  $V_\phi$  with  $[\text{Fe}/\text{H}]$  but they have generally obtained a steeper gradient than our value

$$\frac{\partial V_\phi}{\partial [\text{Fe}/\text{H}]} \approx 5 \text{ km s}^{-1} \text{ dex}^{-1} \quad (\text{old stars}). \quad (6)$$

Measurements from the literature range from  $42 \text{ km s}^{-1} \text{ dex}^{-1}$  to  $51 \text{ km s}^{-1} \text{ dex}^{-1}$ . The literature values are much larger than ours, probably because they refer to samples of thick disc stars (selected chemically, kinematically, or spatially), whereas we have imposed no such selection.

Figure 8 shows the distribution of young (blue) and old (red) stars in the  $(-V_R, V_\phi)$  plane, which is the natural extension of the traditional  $(U, V)$  plane. The histograms in the left and central columns of Fig. 7 are projections of these distributions onto the  $V_R$  and  $V_\phi$  axes. In Fig. 8 metallicity increases from left to right. Literature values for local maxima associated with the Hercules (cyan cross), Hyades (magenta square), and Pleiades (green triangle) moving groups are overplotted (Dehnen 2000; Binney & Tremaine 2008).

The peak in the distribution of young stars moves up and to the right with decreasing metallicity, as we expect given that for these stars  $\partial V_\phi / \partial [\text{Fe}/\text{H}] < 0$  and  $\partial V_R / \partial [\text{Fe}/\text{H}] > 0$ . With the possible exception of the Hercules stream (cyan cross) the contours do not provide convincing evidence for the streams detected by Dehnen (2000) in Hipparcos data. Curiously, the signature of the Hyades stream is most convincing for the most metal-poor Bins 4 and 8. Given the small size of the sample of old stars, and the way the red contours change from one metallicity panel to another, we conclude that these wiggles probably owe more to noise than moving groups.

The histograms for  $V_z$  in the right column of Fig. 7 show that, as expected, the old stars are vertically hotter than the young stars. Whereas for the old stars  $\sigma_z$  tends to increase with decreasing metallicity, from  $\sigma_z = 19.0 \pm 1.2 \text{ km s}^{-1}$  for Bin 5 to  $\sigma_z = 27.3 \pm 1.0 \text{ km s}^{-1}$  for Bin 8,  $\sigma_z$  is essentially independent of metallicity for the young stars. The increase for old stars in  $\sigma_z$  with decreasing  $[\text{Fe}/\text{H}]$ , like the decrease in  $V_\phi$  with decreasing  $[\text{Fe}/\text{H}]$ , points to old, metal-poor stars being on highly eccentric orbits that are not tightly confined to the plane.

### 3.3 Velocity trends with $R$

We now consider kinematic trends with Galactocentric radius. In Figures 9 and 10, we show  $V_R, V_\phi, V_z$  as functions of  $R$  for the young and old stars, respectively. Metal-rich bins are shown in darker colours with thicker lines, with successively lighter colours and thinner lines indicating decreasing metallicity. The plotted values are calculated as follows. The stars in a given age-metallicity bin were ordered by  $R$  and then a window containing  $N$  stars was moved along the resulting lineup, and the mean of  $V_R$ , etc., was computed at each location of the window. This operation was carried out for 1000 values of  $N$  that were drawn from a uniform distribution with a minimum of 20, and a maximum which varied as a function of the size of the age-metallicity bin. The results were then averaged. Average uncertainties for each velocity component are given in their respective panels. The uncertainty in  $R$  largely correlates with the range in Galactocentric radius sampled, and is of the order of  $\sim 0.03$  and  $\sim 0.01 \text{ kpc}$  for young and old stars, respectively.

To check that this procedure generates velocity gradients that are consistent with published gradients, we used it to compute velocity gradients for (i) the complete set of turnoff stars, i.e. all stars in the red dashed rectangle of Figure 3, regardless of age or metallicity, and (ii) the set of red giant stars ( $2 < \log g < 2.5$ ) that satisfy the quality criteria given in Section 2.4.1. For the turnoff stars we find  $\partial V_R / \partial R = -5.7 \pm 2.0 \text{ km s}^{-1} \text{ kpc}^{-1}$ , while for the giant stars  $\partial V_R / \partial R = -5.4 \pm 2.1 \text{ km s}^{-1} \text{ kpc}^{-1}$ . Both of these values agree well with literature values:  $-3 \text{ km s}^{-1} \text{ kpc}^{-1}$  from



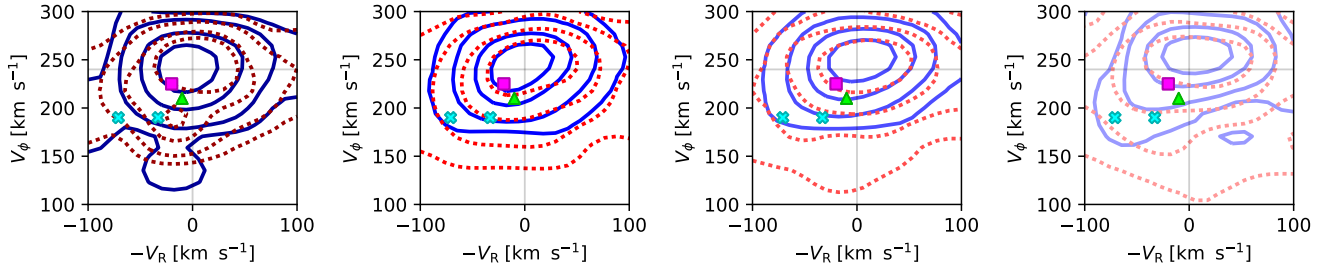


**Figure 8.**  $-V_R; V_\phi$  space for our sample of young (blue, solid) stars and old (red, dashed) stars, split into the four metallicity bins shown in Figure 6. Contours show the density distributions for 33, 67, 90, and 99 per cent of the sample for each bin. The most metal-rich bin ( $0.15 \leq [\text{Fe}/\text{H}] < 0.45$ ) is on the left, and the most metal-poor bin ( $-0.75 \leq [\text{Fe}/\text{H}] < -0.45$ ) is on the right. Cyan crosses indicate the two peaks in the kinematics of the Hercules moving group. The Hyades and Pleiades moving groups are indicated with a magenta square and a green triangle, respectively.

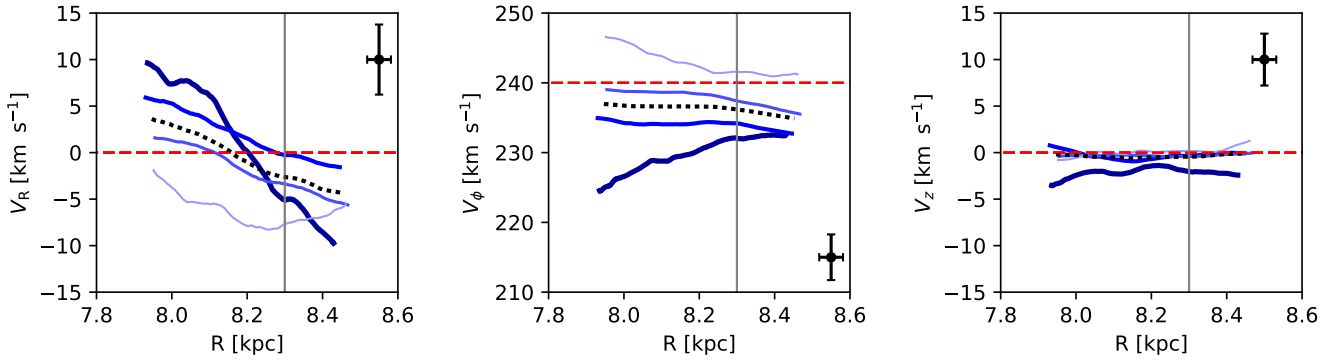


**Figure 9.** Velocity trends as a function of Galactocentric radius (left to right:  $V_R, V_\phi, V_z$ ), weighted by the selection function, for our young stars. The trend for the entire young sample ( $-0.75 \leq [\text{Fe}/\text{H}] < 0.45$ ) is indicated with the black dotted line. The most metal-rich bin ( $0.15 \leq [\text{Fe}/\text{H}] < 0.45$ ) is indicated with the thick, dark blue line, and the most metal-poor bin ( $-0.75 \leq [\text{Fe}/\text{H}] < -0.45$ ) with the thin, light blue line. The solid grey line indicates the position of the Sun. Average uncertainties are indicated in each panel by the error bar.

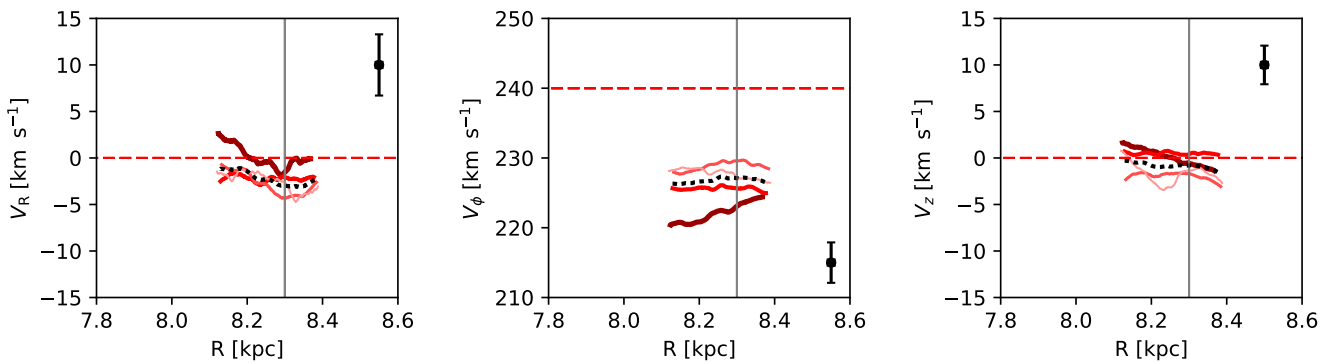


**Figure 10.** Velocity trends as a function of Galactocentric radius (left to right:  $V_R, V_\phi, V_z$ ), weighted by the selection function, for our old stars. The trend for the entire old sample ( $-0.75 \leq [\text{Fe}/\text{H}] < 0.45$ ) is indicated with the black dotted line. The most metal-rich bin ( $0.15 \leq [\text{Fe}/\text{H}] < 0.45$ ) is indicated with the thick, dark red line, and the most metal-poor bin ( $-0.75 \leq [\text{Fe}/\text{H}] < -0.45$ ) with the thin, light pink line. The solid grey line indicates the position of the Sun. Average uncertainties are indicated in each panel by the error bar.

**Table 2.** Measured radial velocity gradients for each age group and metallicity bin.

Bin Number	Metallicity range	$\partial V_R / \partial R$ $\text{km s}^{-1} \text{ kpc}^{-1}$
<b>Young</b>		
1	$0.15 \leq [\text{Fe}/\text{H}] < 0.45$	$-28.0 \pm 9.9$
2	$-0.15 \leq [\text{Fe}/\text{H}] < 0.15$	$-10.6 \pm 3.8$
3	$-0.45 \leq [\text{Fe}/\text{H}] < -0.15$	$-10.2 \pm 3.6$
4	$-0.75 \leq [\text{Fe}/\text{H}] < -0.45$	$-3.6 \pm 1.3$
all	$-0.75 \leq [\text{Fe}/\text{H}] < 0.45$	$-11.4 \pm 4.0$
<b>Old</b>		
5	$0.15 \leq [\text{Fe}/\text{H}] < 0.45$	$-5.9 \pm 2.5$
6	$-0.15 \leq [\text{Fe}/\text{H}] < 0.15$	$-0.7 \pm 1.1$
7	$-0.45 \leq [\text{Fe}/\text{H}] < -0.15$	$-9.9 \pm 4.2$
8	$-0.75 \leq [\text{Fe}/\text{H}] < -0.45$	$-6.8 \pm 2.8$
all	$-0.75 \leq [\text{Fe}/\text{H}] < 0.45$	$-5.9 \pm 2.6$

Siebert et al. (2011),  $-8 \text{ km s}^{-1} \text{ kpc}^{-1}$  from Williams et al. (2013), and  $-6.6 \pm 0.7 \text{ km s}^{-1} \text{ kpc}^{-1}$  from Bovy (2017). Negative values of  $\partial V_R / \partial R$  signal that we lie in a region in which the stellar fluid is being compressed as stars at both smaller and larger radii are moving towards us.

### 3.3.1 Young stars ( $0 < \tau < 3 \text{ Gyr}$ )

The dashed black lines in Figure 9 show the velocity trends for our entire sample of young stars, summed over all four metallicity bins. The gradient of the curve in the panel for  $V_R$  is  $\partial V_R / \partial R = -11.4 \pm 4.0 \text{ km s}^{-1} \text{ kpc}$ . When the sample is decomposed by metallicity, the gradient  $\partial V_R / \partial R$  of the most metal-rich bin (1) is markedly steeper ( $-28.0 \pm 9.9 \text{ km s}^{-1} \text{ kpc}^{-1}$ ) than those of Bins 2 and 3. The curve  $V_R(R)$  for the most metal-poor bin (4) shifts from a negative gradient at smaller radii to a positive gradient at the largest values of  $R$ . The gradients we obtain for Bins 1, 2, and 3 are all steeper than typical literature values for more inhomogeneous populations ( $\lesssim -3 \text{ km s}^{-1} \text{ kpc}$  from Siebert et al. (2011);  $-8 \text{ km s}^{-1} \text{ kpc}^{-1}$  from Williams et al. (2013);  $-6.6 \pm 0.7 \text{ km s}^{-1} \text{ kpc}^{-1}$  from Bovy (2017);  $-7.01 \pm 0.61 \text{ km s}^{-1} \text{ kpc}^{-1}$ , and  $-9.42 \pm 1.77 \text{ km s}^{-1} \text{ kpc}^{-1}$  from Carrillo et al. (2018) for measurements made below and above the plane of the disc, respectively).

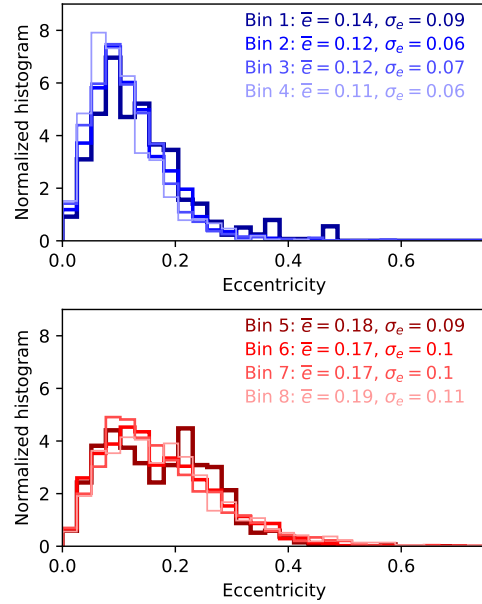
The central panel of Fig. 9 displays again the familiar result that at any radius  $V_\phi$  decreases with increasing  $[\text{Fe}/\text{H}]$  (upper central panel of Fig. 7). The new result we take from Fig. 9 is that the sign of  $\partial V_\phi / \partial R$  changes from positive for the metal-rich Bin 1 to negative for the metal-poor Bin 4. This trend among our young stars is consistent with a finding of Rojas-Arriagada et al. (2016, their Figure 8) for the thin disc as a whole.

The right panel of Fig. 9 shows that  $V_z$  is consistent with zero at all radii for all metallicity bins.

### 3.3.2 Old stars ( $8 < \tau < 13 \text{ Gyr}$ )

Figure 10 shows the dependence of  $\mathbf{V}$  on  $R$  for old stars. Unfortunately, the old stars probe a significantly smaller range in  $R$  than do the young stars.

When all four metallicity bins are aggregated, we obtain a negative gradient,  $\partial V_R / \partial R = -5.9 \pm 2.6 \text{ km s}^{-1} \text{ kpc}^{-1}$ .

**Figure 11.** Orbital eccentricities for our sample of young (top) and old (bottom) stars. Bins in metallicity are defined in Section 2.4.2.

There is a suggestion that the mean value of  $V_R$  decreases with decreasing metallicity, but there is no evident variation of  $\partial V_R / \partial R$  with metallicity, contrary to what we found for the young stars.

All four metallicity bins of old stars have lagging values of  $V_\phi \sim -14 \text{ km s}^{-1}$ , as we expect given the relatively large velocity dispersions of these populations. Any dependence on metallicity of the gradient  $\partial V_\phi / \partial R$  is, for the most part, lost in the noise, contrary to what we found for the young stars. However, we do find that the most metal-rich bin (5) has the greatest lag, similar to Bin 1 for young stars.

The old stars, like the young stars, show no systematic dependence of  $V_z$  on either metallicity or radius, and for all populations  $V_z$  is consistent with zero.

## 4 ORBITAL PARAMETERS

An orbit in the MWPotential2014 potential was computed for each star using the GALPY (Bovy 2015) python package. From the orbit we tabulated the eccentricity  $e$ , guiding radius ( $R_G$ ), and the maximum height above the plane  $z_{\text{max}}$ .

### 4.0.1 Eccentricities

In Figure 11, we show the eccentricity distributions for our young (left panel) and old stars (right panel), divided into bins of metallicity and weighted by the factors  $w_i$  defined in Section 3.1. When all four metallicity bins are aggregated, the eccentricity distribution of our young stars peaks at  $\bar{e} = 0.12$  and has dispersion  $\sigma_e = 0.07$  (typical of the thin disc). The mean value of  $e$  shifts to smaller values with decreasing metallicity ( $\bar{e} = 0.14$  for Bin 1 and  $\bar{e} = 0.11$  for Bin 4), and the dispersion of  $e$  decreases slightly with decreasing metallicity.

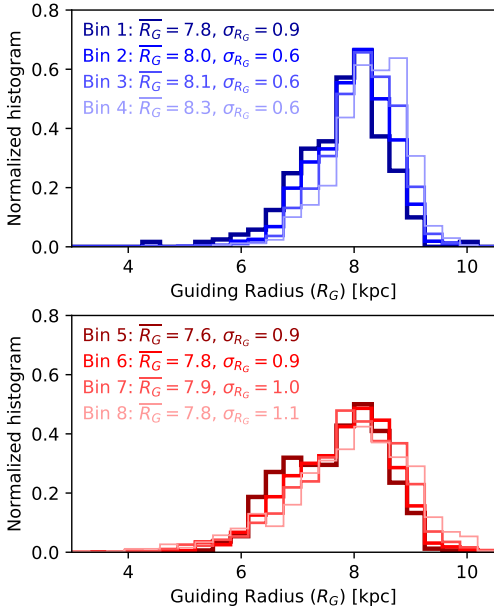


**Figure 12.** Maximum height above the plane ( $Z_{\max}$ ) for our sample of young (top) and old (bottom) stars. Bins in metallicity are defined in Section 2.4.2.

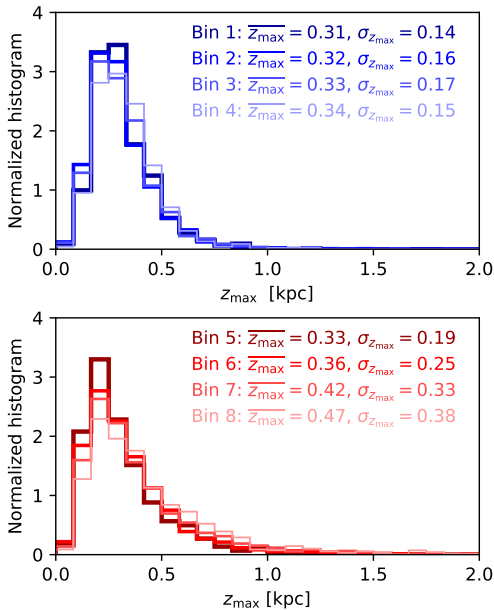


**Figure 13.** Maximum height above the plane ( $Z_{\max}$ ) for our sample of young (top) and old (bottom) stars. Bins in metallicity are defined in Section 2.4.2.

The old stars have a much broader distribution in  $e$ , and consequently a larger mean eccentricity. When the metallicity bins are aggregated, the mean eccentricity of old stars is  $\bar{e} = 0.18$  and its dispersion is  $\sigma_e = 0.1$  (typical of the thick disc, see Kordopatis et al. 2011). In contrast to the young population, the mean and dispersion of the eccentricity distributions are very similar, and slightly increase with decreasing metallicity: the mean  $e$  increases from  $\bar{e} = 0.18$

for Bin 5 to  $\bar{e} = 0.19$  for Bin 8. We note that for the most metal-rich bin ( $0.15 \leq [\text{Fe}/\text{H}] < 0.45$ ), the histogram is suggestive of a bimodality in the eccentricity distribution. Uncertainties in  $\bar{e}$  and  $\sigma_e$  are of the order  $\sim 0.01$ .

#### 4.0.2 Guiding radii

The distributions of guiding radii for our young and old samples are shown in Figure 12. Young stars have mean guiding radii closer to the solar neighbourhood ( $\bar{R}_G = 7.8 - 8.3$  kpc) compared to old stars, which have guiding radii towards the inner disc ( $\bar{R}_G = 7.6 - 7.9$  kpc). The dispersion in guiding radii is also larger for old stars. We also note a hint of a bimodality in the guiding radii distribution for old, metal-rich stars, similar to their eccentricity distribution. In addition, for young stars, we find an increase in guiding radii as a function of decreasing metallicity, corresponding to the results shown in Figure 11. Uncertainties in  $\bar{R}_G$  and  $\sigma_{R_G}$  are of the order  $\sim 0.03$  kpc.

#### 4.0.3 Maximum height above the plane

In Figure 13, we show the distributions of  $z_{\max}$  for our young and old stars. All metallicity bins of young stars have similar means ( $\bar{z}_{\max} = 0.31 - 0.34$  kpc). For young stars, uncertainties on  $\bar{z}_{\max}$  and  $\sigma_{z_{\max}}$  are of the order  $\sim 0.01$  kpc. By contrast the old stars show a significant difference in mean  $Z_{\max}$  between the most metal-rich (Bin 5,  $\bar{z}_{\max} = 0.3$  kpc), and the most metal-poor bin ( $\bar{z}_{\max} = 0.52$  kpc). Uncertainties on  $\bar{z}_{\max}$  and  $\sigma_{z_{\max}}$  for old stars are of the order  $\sim 0.02$  kpc.

The distributions of  $z_{\max}$  for young and old stars are remarkably similar. Both are very skew, but the distribution for old stars has a much stronger tail towards high  $z_{\max}$ . In interpreting these distributions of  $z_{\max}$  it must be borne in mind that RAVE's sightlines avoid the plane, so stars tend to be observed at significant values of  $z$ . Clearly  $z_{\max} \geq z$ . Given the strong correlation of  $\sigma_z$  with age established in earlier work (e.g. Casagrande et al. 2011), most of the youngest stars in the disc have no chance of entering the RAVE catalogue because they do not move far enough from the plane. That is, RAVE must be catching only the high- $V_z$  tail of the youngest stars.

## 5 DISCUSSION AND CONCLUSIONS

The release of Gaia-based parallaxes for the majority of RAVE stars has significantly enhanced the value of the RAVE catalogue by reducing errors in distances and proper motions, particularly for main-sequence and turnoff stars. The new parallaxes also make it possible to determine credible ages for stars in the turnoff region. It is well established that the kinematics of a stellar population is correlated with age and chemistry. Since these correlations arise from the secular evolution of the Galaxy's mass distribution, star-formation rate and non-axisymmetric features (e.g. Aumer et al. 2016; Schönrich & McMillan 2017), they must encode valuable information about our Galaxy's history. Hence it is interesting to re-examine the kinematics-age-metallicity nexus for turnoff stars that appear in both the RAVE and TGAS catalogs.

Unfortunately, even for stars in the RAVE-TGAS overlap, ages are quite uncertain, so we have restricted the analysis to the youngest ( $\tau < 3$  Gyr) and oldest ( $\tau > 8$  Gyr) stars in the expectation that the given uncertainties cannot scatter stars from one extreme group to the other. A corollary of this restriction is that the studied samples are rather small: 6630 young stars and 5072 old stars. We note that while we expect our young stars to be relatively free of contamination, the same cannot be said for the old stars, where we estimate  $\sim 27$  per cent have true ages less than 6 Gyr.

A feature of samples drawn from RAVE that one must always bear in mind is that few RAVE stars lie close to the plane, and distance from the Sun and distance from the plane are correlated. These features arise because RAVE avoids sight lines at low Galactic latitudes. A significant corollary for our sample of young stars is that they must all be outliers in the true distribution of vertical energy and they may not be typical of young stars as a whole.

While the young stars cover a range  $\sim 0.5$  kpc in  $R$ , the sample of old, less luminous stars, has not much more than half the radial range. Consequently, it is hard to establish radial trends for the old stars.

We have used hot turnoff stars to conduct our analysis, and here we note a small caveat regarding RAVE turnoff stars and their derived distances. Kunder et al. (2017) found that distances to RAVE's hot dwarfs in DR5 were some of the most problematic, and an erroneous distance can result in motion associated with differential rotation artificially enhancing values derived for  $V_R$  (Schönrich et al. 2012). However, McMillan et al. (2017), using TGAS parallaxes as a prior to provide updated distance measurements, found that systematic uncertainties were greatly reduced for turnoff stars (see their Section 7). Therefore, while we cannot be completely sure that these results are not artifacts induced by systematic errors in the distances to these hot turnoff stars, we have little reason to believe that our results are simply due to systematics.

Overall, we find negative radial velocity gradients as a function of Galactocentric radii, and measure steeper gradients than those found before for RAVE stars (Siebert et al. 2011; Williams et al. 2013). The source of the negative gradient in  $\partial V_R / \partial R$  is typically attributed to flows induced by non-axisymmetries in the disc (i.e., the bar and/or spiral arms, Siebert et al. 2011, 2012). When we split each age group into bins of metallicity, we show, for the first time, that  $\partial V_R / \partial R$  steepens with metallicity. While a signature of this trend is found in both the young and old stars, it is much more pronounced for young stars.

A possible physical interpretation for this difference may be found by revisiting the  $-V_R; V_\phi$  plane (Figure 8, analogous to the  $U; V$  plane). We recall that moving groups in the local velocity field have been associated with the effects of resonant gravitational interactions due to non-axisymmetries in the MW disc, e.g. the Hercules moving group is typically explained as a signature of a bar that perturbs the orbits of stars near its OLR (e.g. Dehnen 2000; Fux 2001), and the Hyades moving group is typically associated with spiral structure (Quillen & Minchev 2005). Figure 8 shows that for our sample, stars with similar kinematics to those of the Hyades and Hercules moving groups are seen in all metallicity bins and ages. However, we find that the central peak of the distribution for young stars

shifts towards larger values of  $-V_R; V_\phi$  as metallicity decreases. This shift in the peak of the kinematics of young stars may indicate that the relative contribution of each non-axisymmetric component of the disc (the spiral arms and bar, respectively) to the perturbed stellar kinematics varies as a function of metallicity. We note that this correlation also corresponds, as expected, to the observed metallicity gradient in the Galaxy (of the order  $\partial[\text{Fe}/\text{H}]/\partial R \sim -0.06$  dex kpc $^{-1}$ , Boeche et al. 2013; Genovali et al. 2014).

The presence of young, metal-rich stars with similar kinematics as the Hyades moving group is consistent with the results of Quillen & Minchev (2005); Famaey et al. (2008); Antoja et al. (2017), who found the moving group to be metal-rich and produced through gravitational interactions with spiral arms. In addition, the fact that we see these metal-rich stars visiting the solar neighborhood from the inner disc, with similar kinematics as the Hercules moving group, suggests that these stars may have had their orbits affected by similar dynamical interactions with the central bar (Ramya et al. 2016; Antoja et al. 2017). Taking these points into account, we suggest that dynamical effects due to both the bar and spiral arms contribute to the steeper radial velocity gradient we find for young, metal-rich stars, while the more metal-poor stars are less affected by the bar. Our findings are then roughly consistent with Monari et al. (2017, see their Figure 4), where moving further from the OLR decreases the contribution of the bar, similar to what we find for our more metal-poor stars.

We also find secure results regarding the variation of  $V_\phi$  with age, metallicity and Galactocentric radius. All the old populations show a significant lag of  $V_\phi$  relative to the circular speed, with little dependence on metallicity. Among the young stars, it is the most metal-rich that show the greatest lag in  $V_\phi$ , which is a manifestation of the metallicity gradient in the thin disc and epicyclic motions of stars. The most metal-rich subsample of young stars shows rather surprising trends with  $R$  in both  $V_R$  and  $V_\phi$ : its value for  $\partial V_R / \partial R$  is much more negative than the values we obtain for the less metal-rich parts of the young sample, and its value for  $\partial V_\phi / \partial R$  is strongly positive while the more metal-weak young stars show weakly negative values.

We find that the super-solar metallicity young stars have, on average, lower eccentricities than the super-solar metallicity old stars, pointing towards the possibility that the latter have migrated from much further in the Galactic disc. This result adds another dimension (age) to the findings of Kordopatis et al. (2015), where they show that super metal-rich (SMR) stars in the solar neighborhood are on relatively circular orbits. They conclude that these SMR stars must be predominantly affected by resonant scattering at the OLR of the spiral arms (churning, Sellwood & Binney 2002), as their orbital angular momentum has increased to bring them to the solar neighbourhood, without a corresponding increase in eccentricity. We also note the bimodality in the eccentricity and guiding radii distributions for old, metal-rich stars, and suggest that this may be a possible signature of the different processes which bring them to the solar radius—either through epicyclic motions (i.e., stars with larger guiding radii which are temporarily visiting the solar neighbourhood), or churning (true migrators from the inner Galaxy).



With Gaia DR2<sup>2</sup> and additional individual chemical abundances (Wyse et al., in prep), precise age estimates of these stars should allow for observational constraints on the relative efficiency of processes which bring them to the solar neighbourhood.

## ACKNOWLEDGEMENTS

We thank the anonymous referee for their suggestions that greatly improved the quality of the manuscript. We also thank Alice Quillen, Friedrich Anders, and Kyle Oman for their comments and enlightening discussions. Funding for this work and for RAVE has been provided by: the Australian Astronomical Observatory; the Leibniz-Institut für Astrophysik Potsdam (AIP); the Australian National University; the Australian Research Council; the European Research Council under the European Union's Seventh Framework Programme (Grant Agreement 240271 and 321067); the French National Research Agency; the German Research Foundation (SPP 1177 and SFB 881); the Istituto Nazionale di Astrofisica at Padova; The Johns Hopkins University; the National Science Foundation of the USA (AST-0908326); the W. M. Keck foundation; the Macquarie University; the Netherlands Research School for Astronomy; the Natural Sciences and Engineering Research Council of Canada; the Slovenian Research Agency; the Swiss National Science Foundation; the Science & Technology Facilities Council of the UK; Opticon; Strasbourg Observatory; and the Universities of Groningen, Heidelberg and Sydney. The RAVE web site is at <https://www.rave-survey.org>. This work has made use of data from the European Space Agency (ESA) mission *Gaia* (<https://www.cosmos.esa.int/gaia>), processed by the *Gaia* Data Processing and Analysis Consortium (DPAC, <https://www.cosmos.esa.int/web/gaia/dpac/consortium>). Funding for the DPAC has been provided by national institutions, in particular the institutions participating in the *Gaia* Multilateral Agreement.

## REFERENCES

Adibekyan V. Z., et al., 2013, *A&A*, **554**, A44  
 Antoja T., Figueras F., Torra J., Valenzuela O., Pichardo B., 2010, Lecture Notes and Essays in Astrophysics, **4**, 13  
 Antoja T., Figueras F., Romero-Gómez M., Pichardo B., Valenzuela O., Moreno E., 2011, *MNRAS*, **418**, 1423  
 Antoja T., et al., 2015, *ApJ*, **800**, L32  
 Antoja T., et al., 2017, *A&A*, **601**, A59  
 Aumer M., Binney J., Schönrich R., 2016, *MNRAS*, **462**, 1697  
 Bailer-Jones C. A. L., et al., 2013, *A&A*, **559**, A74  
 Binney J., Tremaine S., 2008, Galactic Dynamics: Second Edition. Princeton University Press  
 Binney J., et al., 2014, *MNRAS*, **437**, 351  
 Boeche C., et al., 2011, *AJ*, **142**, 193  
 Boeche C., et al., 2013, *A&A*, **559**, A59  
 Bovy J., 2015, *ApJS*, **216**, 29  
 Bovy J., 2017, *MNRAS*, **468**, L63  
 Bressan A., Marigo P., Girardi L., Salasnich B., Dal Cero C., Rubele S., Nanni A., 2012, *MNRAS*, **427**, 127  
 Carlin J. L., et al., 2013, *ApJ*, **777**, L5

Carrillo I., et al., 2018, *MNRAS*, **475**, 2679  
 Casagrande L., Schönrich R., Asplund M., Cassisi S., Ramírez I., Meléndez J., Bensby T., Feltzing S., 2011, *A&A*, **530**, A138  
 Cutri R. M., et al., 2013, VizieR Online Data Catalog, **2328**  
 De Silva G. M., et al., 2015, *MNRAS*, **449**, 2604  
 Dehnen W., 2000, *AJ*, **119**, 800  
 Famaey B., Pont F., Luri X., Udry S., Mayor M., Jorissen A., 2007, *A&A*, **461**, 957  
 Famaey B., Siebert A., Jorissen A., 2008, *A&A*, **483**, 453  
 Faure C., Siebert A., Famaey B., 2014, *MNRAS*, **440**, 2564  
 Freeman K., Bland-Hawthorn J., 2002, *ARA&A*, **40**, 487  
 Fux R., 2001, *A&A*, **373**, 511  
 Gaia Collaboration et al., 2016, *A&A*, **595**, A1  
 Genovali K., et al., 2014, *A&A*, **566**, A37  
 Gilmore G., et al., 2012, The Messenger, **147**, 25  
 Gómez F. A., Minchev I., O'Shea B. W., Beers T. C., Bullock J. S., Purcell C. W., 2013, *MNRAS*, **429**, 159  
 Górski K. M., Hivon E., Banday A. J., Wandelt B. D., Hansen F. K., Reinecke M., Bartelmann M., 2005, *ApJ*, **622**, 759  
 Grand R. J. J., Kawata D., Cropper M., 2012, *MNRAS*, **421**, 1529  
 Guiglion G., et al., 2015, *A&A*, **583**, A91  
 Holmberg J., Nordström B., Andersen J., 2007, *A&A*, **475**, 519  
 Kapteyn J. C., 1905, Reports of the British Association for the Advancement of Science, 264, 257  
 Kordopatis G., et al., 2011, *A&A*, **535**, A107  
 Kordopatis G., et al., 2013a, *AJ*, **146**, 134  
 Kordopatis G., et al., 2013b, *MNRAS*, **436**, 3231  
 Kordopatis G., et al., 2015, *MNRAS*, **447**, 3526  
 Kordopatis G., Wyse R. F. G., Chiappini C., Minchev I., Anders F., Santiago B., 2017, *MNRAS*, **467**, 469  
 Kunder A., et al., 2017, *AJ*, **153**, 75  
 Kushniruk I., Schirmer T., Bensby T., 2017, preprint, ([arXiv:1709.06905](https://arxiv.org/abs/1709.06905))  
 Lee Y. S., et al., 2011, *ApJ*, **738**, 187  
 Lindegren L., et al., 2016, *A&A*, **595**, A4  
 Majewski S. R., et al., 2017, *AJ*, **154**, 94  
 Matijević G., et al., 2012, *ApJS*, **200**, 14  
 McMillan P. J., 2013, *MNRAS*, **430**, 3276  
 McMillan P. J., et al., 2017, preprint, ([arXiv:1707.04554](https://arxiv.org/abs/1707.04554))  
 Minchev I., Boily C., Siebert A., Bienayme O., 2010, *MNRAS*, **407**, 2122  
 Monari G., Helmi A., Antoja T., Steinmetz M., 2014, *A&A*, **569**, A69  
 Monari G., Famaey B., Siebert A., 2016, *MNRAS*, **457**, 2569  
 Monari G., Famaey B., Fouvry J.-B., Binney J., 2017, *MNRAS*, **471**, 4314  
 Nordström B., et al., 2004, *A&A*, **418**, 989  
 Proctor R. A., 1869, Proceedings of the Royal Society of London Series I, **18**, 169  
 Prusti T., 2012, *Astronomische Nachrichten*, **333**, 453  
 Purcell C. W., Bullock J. S., Tollerud E. J., Rocha M., Chakrabarti S., 2011, *Nature*, **477**, 301  
 Quillen A. C., Minchev I., 2005, *AJ*, **130**, 576  
 Quillen A. C., Dougherty J., Bagley M. B., Minchev I., Comparetta J., 2011, *MNRAS*, **417**, 762  
 Ramya P., Reddy B. E., Lambert D. L., Musthafa M. M., 2016, *MNRAS*, **460**, 1356  
 Recio-Blanco A., et al., 2014, *A&A*, **567**, A5  
 Recio-Blanco A., et al., 2016, *A&A*, **585**, A93  
 Rojas-Arriagada A., et al., 2016, *A&A*, **586**, A39  
 Schönrich R., 2012, *MNRAS*, **427**, 274  
 Schönrich R., McMillan P. J., 2017, *MNRAS*, **467**, 1154  
 Schönrich R., Binney J., Dehnen W., 2010, *MNRAS*, **403**, 1829  
 Schönrich R., Binney J., Asplund M., 2012, *MNRAS*, **420**, 1281  
 Sellwood J. A., Binney J. J., 2002, *MNRAS*, **336**, 785  
 Sharma S., Bland-Hawthorn J., Johnston K. V., Binney J., 2011, *ApJ*, **730**, 3  
 Siebert A., et al., 2011, *MNRAS*, **412**, 2026

<sup>2</sup> <https://www.cosmos.esa.int/web/gaia/dr2>

- Siebert A., et al., 2012, [MNRAS](#), **425**, 2335  
 Skrutskie M. F., et al., 2006, [AJ](#), **131**, 1163  
 Spagna A., Lattanzi M. G., Re Fiorentin P., Smart R. L., 2010, [A&A](#), **510**, L4  
 Steinmetz M., et al., 2006, [AJ](#), **132**, 1645  
 Widrow L. M., Gardner S., Yanny B., Dodelson S., Chen H.-Y., 2012, [ApJ](#), **750**, L41  
 Williams M. E. K., et al., 2013, [MNRAS](#), **436**, 101  
 Wojno J., et al., 2016, [MNRAS](#), **461**, 4246  
 Wojno J., et al., 2017, [MNRAS](#), **468**, 3368  
 Yanny B., et al., 2009, [AJ](#), **137**, 4377  
 Zhao G., Zhao Y.-H., Chu Y.-Q., Jing Y.-P., Deng L.-C., 2012, [Research in Astronomy and Astrophysics](#), **12**, 723

This paper has been typeset from a  $\text{\TeX}/\text{\LaTeX}$  file prepared by the author.